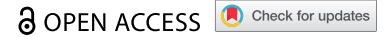


ORIGINAL RESEARCH



## Quantitative MRI cell tracking of immune cell recruitment to tumors and draining lymph nodes in response to anti-PD-1 and a DPX-based immunotherapy

Marie-Laurence Tremblay<sup>a,b,c</sup>, Zoe O'Brien-Moran<sup>a,d</sup>, James A. Rioux<sup>a,d,e</sup>, Andrea Nuschke<sup>a</sup>, Christa Davis<sup>a</sup>, W. Martin Kast<sup>f</sup>, Genevieve Weir<sup>b,c</sup>, Marianne Stanford<sup>b,c</sup>, and Kimberly D. Brewer<sup>a,b,d,e,g</sup>

<sup>a</sup>Biomedical Translational Imaging Centre (BIOTIC), IWK Health Centre, Halifax, NS, Canada; <sup>b</sup>Dalhousie University, Halifax, NS, Canada; <sup>c</sup>IMV Inc, Halifax, NS, Canada; <sup>d</sup>Department of Physics, Dalhousie University, Halifax, NS, Canada; <sup>e</sup>Department of Diagnostic Radiology, Dalhousie University, Halifax, NS, Canada; <sup>f</sup>Keck School of Medicine, University of Southern California, Los Angeles, CA, USA; <sup>g</sup>School of Biomedical Engineering, Dalhousie University, Halifax, NS, Canada

### ABSTRACT

DPX is a unique T cell activating formulation that generates robust immune responses (both clinically and preclinically) which can be tailored to various cancers via the use of tumor-specific antigens and adjuvants. While DPX-based immunotherapies may act complementary with checkpoint inhibitors, combination therapy is not always easily predictable based on individual therapeutic responses. Optimizing these combinations can be improved by understanding the mechanism of action underlying the individual therapies. Magnetic Resonance Imaging (MRI) allows tracking of cells labeled with superparamagnetic iron oxide (SPIO), which can yield valuable information about the localization of crucial immune cell subsets. In this work, we evaluated the use of a multi-echo, single point MRI pulse sequence, TurboSPI, for tracking and quantifying cytotoxic T lymphocytes (CTLs) and myeloid lineage cells (MLCs). In a subcutaneous cervical cancer model (C3) we compared untreated mice to mice treated with either a single therapy (anti-PD-1 or DPX-R9F) or a combination of both therapies. We were able to detect, using TurboSPI, significant increases in CTL recruitment dynamics in response to combination therapy. We also observed differences in MLC recruitment to therapy-draining (DPX-R9F) lymph nodes in response to treatment with DPX-R9F (alone or in combination with anti-PD-1). We demonstrated that the therapies presented herein induced time-varying changes in cell recruitment. This work establishes that these quantitative molecular MRI techniques can be expanded to study a number of cancer and immunotherapy combinations to improve our understanding of longitudinal immunological changes and mechanisms of action.

### ARTICLE HISTORY

Received 31 August 2020  
Revised 11 November 2020  
Accepted 11 November 2020

### KEYWORDS

magnetic resonance imaging (MRI); immunotherapy; anti-PD-1; cytotoxic T lymphocytes (CTLs); myeloid lineage cells (MLCs)


### Introduction

Immunotherapies have had several recent clinical successes, with many more promising therapies studied preclinically or in early-stage clinical trials. Checkpoint inhibitors are some of the most clinically successful immunotherapies to date due to their ability to block immune evasion mechanisms of tumors, hence permitting the immune system to identify, penetrate, and attack cancerous masses.<sup>1–5</sup> Monoclonal antibodies targeting checkpoint molecules, such as anti-PD-1 (nivolumab, pembrolizumab) and anti-CTLA-4 (ipilimumab), are already approved for certain cancers. Checkpoint inhibitors function by preventing the dampening of CD8<sup>+</sup> T cell-mediated cytotoxicity within the tumor.<sup>3</sup> Peptide-based immunotherapies are another promising class of immunotherapies that may be synergistic with checkpoint inhibitors, as these therapies can generate robust, antigen-specific T cell responses.<sup>6</sup> DPX is a unique oil-based formulation that is a T cell activating therapy. It is currently in Phase 2 clinical trials formulated with survivin antigens.<sup>7</sup> Initial results repeatedly demonstrate robust responses (both clinically and preclinically) and can be tailored to various cancers via the use of tumor-specific antigens and adjuvants.<sup>6,8–10</sup>

Unfortunately, although these individual therapies are promising, durable clinical responses are only observed in select patients. It is therefore important to evaluate multiple therapies preclinically. Recent literature increasingly suggests that tumor regression/remission is improved when immunotherapies are administered in combination,<sup>4,11</sup> as these combination therapies are often synergistic, offering increased success over single therapies used in isolation. However, therapy optimization is complex and likely cancer specific, with multiple factors affecting efficacy such as treatment order and timing. Therapy combination is not always easily predictable based on individual therapeutic responses.<sup>12,13</sup> Therapies must be strategically administered, and the treatment course carefully monitored and well characterized at the early stages of development. It is crucial that we broaden the range of tools being used in pre-clinical studies to increase our understanding of immunotherapy mechanisms of action.

Molecular imaging is an important tool for monitoring immunotherapy treatments and outcomes. It allows longitudinal characterization and monitoring of individual immune environments in response to both cancer and therapy. Given the highly variable and individualized nature of immunotherapy, imaging offers valuable opportunities to longitudinally

**CONTACT** Kimberly D. Brewer  [brewerk@dal.ca](mailto:brewerk@dal.ca)  Biomedical Translational Imaging Centre (BIOTIC), IWK Health Centre, Halifax, NS.

 Supplemental data for this article can be accessed on the [publisher's website](#).

© 2020 The Author(s). Published with license by Taylor & Francis Group, LLC.

This is an Open Access article distributed under the terms of the Creative Commons Attribution-NonCommercial License (<http://creativecommons.org/licenses/by-nc/4.0/>), which permits unrestricted non-commercial use, distribution, and reproduction in any medium, provided the original work is properly cited.

assess individual-level responses. Imaging can also be used in mouse models, where there is often significant intra-group variability in therapy response even in genetically identical mice.<sup>13,14</sup> While far from perfect, the mouse model does reflect a portion of the diversity and variability within human populations, particularly in the tumor microenvironment and immune system heterogeneity. Imaging is also an important tool for developing and testing novel therapeutic compounds both preclinically and clinically. However, while imaging technology has progressed rapidly and offers opportunities to study immunotherapies,<sup>14–19</sup> wider implementation of these methods remains limited.

Magnetic Resonance Imaging (MRI) is a useful tool for tracking cells labeled with superparamagnetic iron oxide (SPIO), which can yield valuable information about the localization of crucial immune cell subsets. MRI has been used by a number of groups to follow adoptive transfer of immune cells that are used as a therapy, such as cytotoxic T lymphocytes (CTLs) or dendritic cells (DCs), general myeloid lineage cells (MLCs), or to track macrophages in the tumor microenvironment.<sup>16,20–23</sup> MRI cell tracking can be used to understand the dynamic changes of individual responses to immunotherapy in the tumor microenvironment. While flow cytometry and immunohistochemistry can offer valuable and important information during studies from peripheral samples, localized biopsies, or via *ex vivo* sampling after study completion, they have limitations. Unlike MRI cell tracking, these methods do not allow longitudinal sampling of the complex heterogeneity across a single tumor, or across multiple tumor sites, nor do they allow longitudinal monitoring of other important organs such as lymph nodes.

However, immune cell tracking for the purpose of exploring non-cell-based therapies is still in its infancy. One limiting factor is the difficulty in obtaining quantitative data. Most MRI cell tracking studies using SPIO as a contrast agent result in either purely qualitative assessments of cell migration<sup>24,25</sup> or use a semi-quantitative metric requiring a pre-scan acquired prior to injection of cells,<sup>26,27</sup> which doubles imaging time. Some studies have used <sup>19</sup>F probes as cell labels to avoid these limitations because <sup>19</sup>F-labeled cells are fully quantitative and more specific.<sup>16,21</sup> The downside of <sup>19</sup>F probes is that they have a much lower sensitivity, especially at lower field strengths, which in turn limits the numbers of cells that can be tracked.

We propose the use of a multi-echo, single point MRI pulse sequence, TurboSPI.<sup>28,29</sup> TurboSPI functions by sampling the iron-induced signal decay in each voxel with a high temporal resolution, from which cell concentrations can be derived. In contrast to traditional biological and/or histological methods, TurboSPI MRI enables repeated quantitative monitoring of the same region in the same individual mouse over time. It also does not require the use of a pre-scan prior to cell injection and delivers quantitative metrics via a modified form of  $R_2^*$  mapping. Importantly, TurboSPI is insensitive to freely circulating iron, due to the nature of signal decay induced by SPIO within cells vs. free iron, while maintaining sensitivity to a large dynamic range of SPIO-labeled cells.

Previous work by Weir et al.<sup>30</sup> demonstrated that the combination of anti-PD-1 with DPX-based targeted immunotherapy significantly increased antigen-specific tumor-infiltrating

lymphocytes (TILs) and increased the total number of CD8 + TILs in a murine model of cervical cancer. We, therefore, chose this model to evaluate TurboSPI MRI as a potential tool for quantitative *in vivo* evaluation of longitudinal cell recruitment changes, which, once properly tested, has the potential to be used more closely to investigate longitudinal mechanistic changes in immune cells *in vivo*.

In this work, we evaluated how TurboSPI MRI can be used to quantitatively and qualitatively evaluate the recruitment of both CTLs and MLCs in a murine preclinical model. Mice were either left untreated as a control, treated with anti-PD-1, DPX-R9F (where R9F is the HPV16 E7 antigen that has been demonstrated to be immunodominant in this model), or both in combination. Two immune cell populations (MLCs and CTLs) were adoptively transferred and the recruitment of immune cells to the tumor and inguinal lymph nodes was evaluated at two different time points. Our results indicated that it is possible to detect differences with TurboSPI in CTL recruitment in response to combination therapy and differences in MLC recruitment to lymph nodes in response to therapy. Additionally, we demonstrated that therapies induced time-dependent changes in cell recruitment.

## Methods

### Mice

Female C57BL/6 mice (6–8 weeks old, pathogen free) obtained from Charles River Laboratories (St. Constant, PQ) were used as recipient mice of adoptive cell transfer (ACT). C57BL/6-Tg (Ubc-GFP)30Scha/J mice (B6-GFP+; Jackson Laboratories) were bred in-house and females (6–16 weeks old) were used as donor mice for cell isolation, culture, and SPIO labeling. All mice were housed at the IWK Animal Care Facility with food and water *ad libitum* under filter top conditions. Experiments involving the use of mice were carried out in accordance with protocols approved by the University Committee on Laboratory Animals at Dalhousie University, Halifax, NS, Canada.

### Cancer cell line

The murine cervical cancer C3 cell line<sup>31</sup> (obtained from Dr. Martin Kast; cryopreserved in fetal bovine serum (FBS) + 10% dimethylsulfoxide in liquid nitrogen) was maintained in complete DMEM (cDMEM); DMEM (Corning) supplemented with 10% FBessence (Seradigm), 5 mM L-glutamine (Gibco), Penicillin/streptomycin (Gibco), 5 mM of  $\beta$ -mercaptoethanol (Gibco) and kept at 37°C in a standard incubator in 5% CO<sub>2</sub> atmosphere.

### Immunotherapies

DPX-R9F was prepared at IMV Inc. (Halifax, NS) using their proprietary DPX platform described previously.<sup>27</sup> Briefly, DPX-R9F was formulated by combining the universal T-helper peptide TT<sub>947-967</sub> (FNNFTVSWLRVLPKVSASHLE; F21E) with the CD8 epitope of human papillomavirus-16 E7<sub>49-57</sub> (RAHYNIVTF; R9F) specific to the C3 cancer epitope in a lipid mixture of phosphatidylcholine and cholesterol in

a 10:1 w/w ratio (Lipoid GmbH, Ludwigshafen, Germany) and a proprietary polynucleotide-based adjuvant. The lyophilized mixture was reconstituted in Montanide ISA 51 VG (Seppic S. A., Paris, France).<sup>6,27,30,32</sup> Each dose of 50  $\mu$ L DPX-R9F contains 5 mg of R9F, 5 mg of F21E, and 20 mg of the polynucleotide-based adjuvant and was injected subcutaneously in the right flank 15 days post C3 cancer implant. Anti-mouse PD-1 (CD279; clone RMP1-14; BioXCell) was diluted in 1X PBS (Corning) to 200  $\mu$ g/dose of 350  $\mu$ L and injected intraperitoneal 7, 9, 11, 21, and 25 days post C3 cancer implant. See Supplementary Figure 1 for Timeline.

### Tumor challenge

All mice were implanted with  $5 \times 10^5$  C3 cells subcutaneously into the left flank. C57BL/6 mice were divided into four groups: untreated, treated with anti-PD-1, treated with DPX-R9F, or treated with the combination of anti-PD-1 and DPX-R9F ( $n = 5$ /group/labeled immune cell type). Tumor size was measured via calipers on a weekly basis for the first 3 weeks and bi-weekly thereafter. Tumor volumes were calculated using the formula: [(longest measurement  $\times$  shortest measurement)<sup>2</sup>]  $\div$  2. Final tumor volumes were determined postmortem at the last imaging day using MR images. Lymph node, spleen, and tumors were harvested and frozen in OCT:20% sucrose at a 2:1 v/v for immunohistochemistry.

### Cytotoxic T cell isolation and culture

One week prior to cell injection, inguinal, axillary, brachial, and mesenteric LNs were collected from treatment- and disease-matched B6-GFP<sup>+</sup> mice. Cytotoxic T lymphocytes (CTLs) were isolated as previously described.<sup>27</sup> Briefly, CD8<sup>+</sup> lymphocytes were enriched using a panning method. The enriched CTL population was cultured *in vitro* at a density of  $1 \times 10^6$  cells/mL in complete RPMI media (cRPMI) supplemented with mouse CD28 (1  $\mu$ g/mL; clone 37.51; eBiosciences), gentamycin (5  $\mu$ g/mL; Gibco), IL-2 (100 U/mL; Sigma-Aldrich), and IL-12 (100 ng/mL; Sigma-Aldrich) on a coated CD3e (2  $\mu$ g/mL; clone 145-2C11; Tonbo Biosciences) culture flask to encourage cellular proliferation and activation. Five days before ACT, spleens were isolated from disease- and treatment-matched B6 mice and cultured *in vitro* in cDMEM media at 37°C in an incubator to act as antigen-presenting cells to the CTLs. Three days before ACT, splenocyte proliferation was prohibited using mitomycin-c (50  $\mu$ g/mL; Sigma-Aldrich) and after washing, added to the CTL culture at a ratio of 1:10 APC:CTL. R9F (10  $\mu$ g/mL in DMSO; Genscript) was added to encourage further priming. Fresh cRPMI supplemented with 100 U/mL of IL-2 was added and replaced as needed to maintain the CTLs in culture.

### Myeloid lineage cell culture

Bone marrow was isolated from femurs and tibias of treatment- and disease-matched B6-GFP<sup>+</sup> mice, and was incubated in cRPMI supplemented with GM-CSF (20 ng/mL) (Peprotech, USA) at  $3 \times 10^5$  cells/mL. cRPMI supplemented with 20 ng/mL of GM-CSF was added as nutrients were being depleted. Non-

adherent cells were transferred to a new plate 6 days after isolation and media were replenished with 10 ng/mL of GM-CSF. Myeloid lineage cells (MLCs) were stimulated with R9F (20  $\mu$ g/mL) at days 7 and 9 post isolation.

### Cell labeling with SPIO

CTLs were washed and incubated with Molday ION<sup>TM</sup> Rhodamine B SPIO (75  $\mu$ g/mL; 30 nm, BioPal Inc, Worcester, Massachusetts, USA), herein referred to as SPIO, at a density of 4 million cells/mL in cRPMI supplemented with IL-2 (100 U/mL) for 20–24 h. Labeled cells were then washed thoroughly in 1X PBS and resuspended at  $40 \times 10^6$  cells/mL in Hank's Buffered Salt Solution without calcium and magnesium (HBSS; Corning, USA) with 20 mM HEPES buffer (Corning). Each mouse received 8 million CTLs in a 200  $\mu$ L dose in the tail vein. Dendritic cells were incubated with 30  $\mu$ g/mL SPIO at a density of 4 million cells/mL overnight in cRPMI supplemented with 10 ng/mL of GM-CSF. Cells were thoroughly washed in 1X PBS and resuspended at  $5 \times 10^6$  cells/mL in HBSS with 2 mM HEPES buffer. Each mouse received 1 million DCs in a 200  $\mu$ L dose in the tail vein.

### Cell culture phenotyping

Inguinal LNs and tumors were immediately collected from mice after receiving their last MRI scans. Single-cell suspensions of inguinal lymph nodes were prepared by homogenizing the LNs through a 40  $\mu$ m cell strainer. Cell numbers were determined using a hemocytometer. Tumor single-cell suspensions were obtained by digestion of tumors in a solution of HBSS with calcium and magnesium (Gibco) supplemented with 100 mg/mL of collagenase Type I (Gibco) and 50 mg/mL of DNAase I from bovine pancreas (Sigma) for 30 min at 37°C with shaking every 15 min. The digested tumor was then reduced to a single-cell suspension through a 70  $\mu$ m cell strainer and counted. Both tumor and LN cells were washed in 1X PBS and incubated for 30 min with fluorescent antibodies for flow cytometry analysis. CTLs and DC cultures were also evaluated for purity and phenotype. The following anti-mouse antibodies were used for identification of CTLs: CD8 $\alpha$  phycoerythrin (PE) or efluor660 (clone 53-6.7), KLRG1-PE (clone 2F1), PD1-PE or allophycocyanine (APC) (CD279; clone J43), TIM3 (CD366)-PE or APC (clone RMT3-23), and CD3-APC (clone 17A2). For identification of MLCs, the following anti-mouse antibodies were used: CD11 c-PE or APC-eFluor780 (clone N418), CCR7-APC (clone 4B12), CD80-PE (clone B7-1), MHCII-APC (clone 114.15.2). All antibodies were from eBioscience (ThermoFisher). After incubation, cells were washed with 1X PBS and fixed at 4% PFA for 20 min. Data were acquired on a BD FACS Canto II (BD Biosciences, San Jose, CA) and analyzed on FCS Express 6 flow (De Novo Software, Glendale, CA). Cells were gated on lymphocytes using forward and side scatters, then gated for GFP<sup>+</sup> cells and the markers of interest described above.

### Immunofluorescence and microscopy

Immunohistochemistry was performed as previously described.<sup>28</sup> Briefly, tumors and lymph nodes were cryosectioned at  $-20^\circ\text{C}$  with 10  $\mu$ m thickness. Tissues were rehydrated in 1X PBS and fixed with 4% paraformaldehyde for 15 min at room temperature.

Tissues were then blocked with 0.1% bovine serum albumin (Sigma) for 30 min. Tissues of mice that received CTLs were incubated with anti-mouse CD8 $\alpha$  eFluor 660 (clone 53-6.7, eBioscience, ThermoFisher) and tissues of mice that received MLCs were incubated first with purified rat-anti mouse dendritic cell marker (clone 33D1) (BD Biosciences, San Jose, CA) at 1:250 overnight at 4°C then stained with Alexa Fluor 633 goat anti-rat (H + L) at a 1:100 for an hour at 4°C. Slides were mounted with Fluoromount-G (eBioscience, ThermoFisher) containing DAPI for nuclei staining.

Tissues were visualized as described previously.<sup>27</sup> Briefly, a Zeiss LSM 710 laser scanning confocal microscope equipped with an XBO 50 W lamp, argon, and a HeNe lasers for excitation at 365, 488, 548 nm. Images were collected with a 1024  $\times$  1024 pixel resolution, at 1 A.U. with a pixel dwell time of 6.33  $\mu$ sec. Images were visualized and channels separated using Fiji (ImageJ, NIH, US).<sup>33</sup>

### MRI data acquisition and analysis

All data were acquired on a 3 T magnet equipped with a 21-cm i.d. gradient coil (200 mT/m; Magnex Scientific, Oxford, UK) interfaced with a Varian DD console (Varian Inc, Palo Alto, CA, USA). A 30 mm i.d. quadrature transmit/receive RF coil (Doty Scientific, Columbia, SC, USA) was used to image tumors, treatment sites, and inguinal lymph nodes simultaneously. Anatomical images were obtained using a 3D-balanced steady-state free precession (bSSFP) sequence (repetition time/echo time = 8/4 ms, flip angle = 30°, four signal averages) with a field of view (FOV) of 38.4  $\times$  25.5  $\times$  25.5 mm, a 256  $\times$  170  $\times$  170 matrix centered on the lower torso and legs, and 150  $\mu$ m isotropic resolution. SPIO density measurements from labeled injected cells were derived from R<sub>2</sub>\* mapping, data for which are acquired with the multi-echo single point imaging sequence, TurboSPI<sup>28,29</sup> (TR = 250.0 ms, ETL = 8.0 ms, ESP = 10.0 ms, 90° flip angle, FOV of 25  $\times$  25  $\times$  25 mm, 96  $\times$  96  $\times$  48 matrix, 8x acceleration factor). The in-plane resolution is 320  $\mu$ m with 0.5 mm slices. A fast spin-echo image was acquired before TurboSPI to use as a reference for TurboSPI image reconstruction. Mice were imaged on days 21 and 28 post-implant, and ~24 h after SPIO-labeled cell injections, with a scan time of approximately 2 hours per session. Bulk R<sub>2</sub>\* measurements were also acquired on cells (CTLs and MLCs) suspended in gelatin in NMR tubes for calibrating the relationship of R<sub>2</sub>\* to cell density.

### MRI image analysis

Images were all converted to NiFTI files and overlaid in VivoQuant (InVivo, Ma, US) using the anatomical image as the reference and the fast spin-echo image as the reference for R<sub>2</sub>\* maps. Regions of interests (ROI) were drawn on tumor and lymph nodes using the anatomical image in VivoQuant for each imaging time point. ROIs were verified by a separate reviewer. Cell densities in tumors and lymph nodes were obtained by extracting frequency histograms of the R<sub>2</sub>\* signal from the ROIs and imported into a spreadsheet for a quick conversion from R<sub>2</sub>\* values per voxel to cell density per mm<sup>3</sup> using the calibration curve for either CTLs or MLCs.<sup>34</sup> All voxels in the ROI were summed resulting in total cell density for each tumor and lymph node ROI. Data were then imported into

GraphPad Prism 8 (San Diego, CA, US) for statistical analysis. \*Tumor and lymph node volumes and CTL and MLC numbers were assessed using student t-tests with Dunnett's multiple comparison correction. Changes in cell recruitment and time (i.e. study day) in both tumors and LNs for CTLs and MLCs were assessed using the mixed-effects model in Prism 8 (due to missing values, a traditional repeated measures ANOVA was not possible). The relationship between CTL or MC recruitment and tumor volumes was assessed using linear regression analysis in Prism 8.

## Results

### Imaging verifies tumor suppression by DPX-R9F and anti-PD-1 treatment

Volumetric analysis of the tumor and inguinal lymph nodes is shown in Figure 1. Treatment with DPX-R9F, both alone and in combination with anti-PD-1, significantly decreased tumor volumes measured both by calipers (Figure 1a) and MRI ROI analysis (Figure 1b). Interestingly, mice treated with the DPX-based immunotherapy alone had slightly smaller tumors than the combination therapy, though this difference was not significant. We found that caliper measurements generally appeared to slightly overestimate tumor volumes compared to more accurate MRI measurements. There were no statistically significant changes in lymph node volumes (Figure 1c, d) in response to treatment. However, treatment with DPX-R9F, both alone and in combination, appeared to increase volumes of the DPX-R9F draining inguinal lymph node (right LN).

### SPIO labeling does not significantly affect CTL or MLC phenotype

CTLs and MLCs were isolated from treatment- and disease-matched B6-GFP+ mice and cultured *in vitro* for 8–9 days before labeling with SPIO. B6-GFP mice express GFP in all tissues and all immune cells isolated from them are expected to be GFP+. CTLs were consistently ~80–90% CD8 $\alpha$ + and GFP+ (Supplementary Figure 2). Non-labeled CD8 $\alpha$ + cells in the CTL culture are APCs used to prime the T cells. CTL functionality was assessed through the expression of the checkpoint inhibitors PD-1, TIM3, and CTLA-4. There is a 17% increase in PD-1 expression and an 8% increase in TIM3 expression after SPIO labeling. MLCs were ~80% CD11c+ and GFP+ pure, and that ratio did not change after SPIO labeling. There was no major difference between MHCII, CD80, and CCR7 expression after SPIO labeling. Following labeling with SPIO, CTLs were found to have approximately 3 pg iron/cell and MLCs had between 8 and 9 pg iron/cell. In order to acquire accurate TurboSPI maps, R<sub>2</sub>\* calibration curves were generated for both SPIO-labeled MLCs and CTLs (Figure 2b) using labeled cells suspended in gelatin in 5 mm NMR tubes. Quantitative cell density maps were generated from TurboSPI data.

### Treatment with the DPX-based targeted therapy drives CTLs to tumors

SPIO-CTLs were injected into recipient B6 mice on days 20 and 27 post-implant and imaged with MRI 24 hours post-

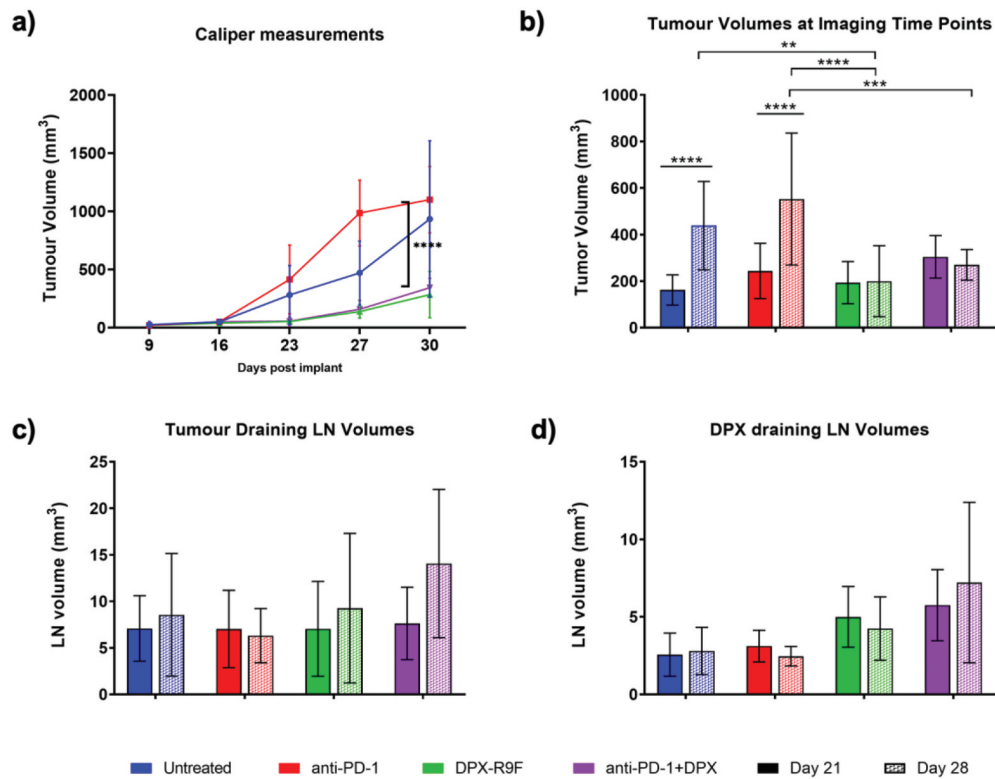


**Figure 1.** Treatment with DPX significantly reduces tumor burden. a) Caliper measurements of tumor volumes throughout the study. b) Tumor volumes as measured by MRI at days 21 and 28. c) & d) Tumor draining lymph node (left LN) and DPX draining lymph node (right LN) volumes as measured by MRI at day 21 and 28. \* indicates significance according to t-test with Dunnett's multiple comparison correction. \*\* is  $p < .05$ , \*\*\* is  $p < .01$ , \*\*\*\* is  $p < .005$ .

injection. The location and number of SPIO-CTLs located within the tumors are shown in Figure 3. As tumors grew larger, they recruited more SPIO-CTLs (Figure 3a, b). There was no significant difference in the recruitment rate (i.e. the slope of the lines in Figure 3a, b) or the total number of SPIO-CTLs present in tumors at either day 21 or day 28 regardless of treatment. However, the cellular density of SPIO-CTLs in the untreated and anti-PD-1 treated mice decreased over time while the number of recruited SPIO-CTLs increased with the combination therapy between day 21 and 28 (Figure 3c). This is better illustrated in Figure 3d, where the SPIO-CTL density clearly decreases over time for anti-PD-1 and untreated mice, has effectively no change with the DPX-R9F therapy and significantly increases ( $p < .1$ ) with the combination therapy. Figure 3e shows representative recruitment maps of CTLs in

both the tumor (top row) and inguinal lymph nodes (bottom row). Treatment did not appear to affect the recruitment patterns, with recruitment primarily located around the periphery of tumors and not localized to any particular region in the lymph nodes.

### MLC migration to tumors changes with treatment

SPIO-MLCs were injected into recipient B6 mice (separate group from CTLs) on days 20 and 27 post-implant and imaged with MRI 24 hours post-injection. The number of SPIO-MLCs recruited to the tumor increased with increasing tumor volumes and this recruitment rate significantly accelerated between days 21 and 28 (Figure 4a, b). At day 21, there were significantly more SPIO-MLCs present in untreated mice

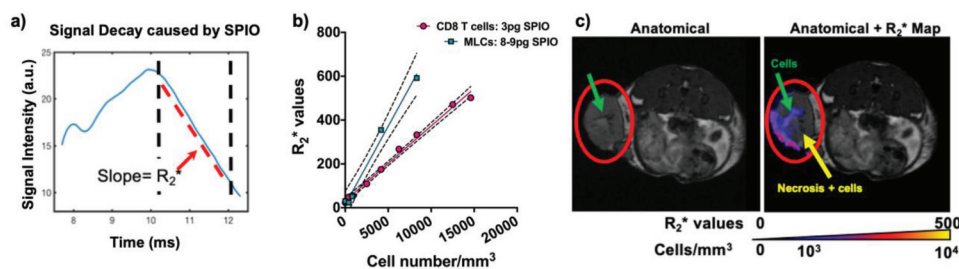


**Figure 2.** TurboSPI  $R_2^*$  mapping of SPIO-labeled immune cells. a) Representative MRI signal readout demonstrating decay from SPIO-labeled cell. Dotted lines indicate region used for calculation of  $R_2^*$  decay. b) Calibration curves calculated for  $R_2^*$  values of SPIO-labeled cells in vitro (including both CD8 T cells and MLCs). Pixel-wise  $R_2^*$  values are calculated (from a) to yield  $R_2^*$  maps which are overlaid on an anatomical image (in c). The calibration curve (in b) is used to convert these values to cellular density in cells/mm<sup>3</sup>. Red circle indicates primary tumor with arrows indicating potential cells and necrotic region.

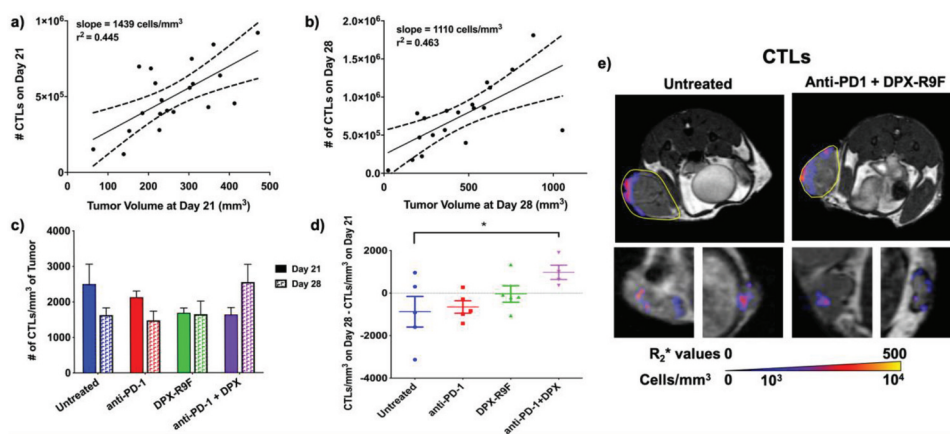


**Figure 3.** Combination therapy increases recruitment of CTLs between day 21 and day 28. a) Individual graph showing numbers of CTLs recruited to the primary tumor at day 21 compared to the tumor volume at day 21. b) Same as A but for day 28. Both graphs in A and B are statistically non-zero according to linear regression analyses. c) The cellular density of CTLs recruited to the primary tumor for each treatment regime at both day 21 and day 28. d) The difference in cellular density of recruited CTLs between day 28 and day 21. \* indicates  $p < .1$  according to t-test with Dunnett's correction for multiple comparisons. e) Representative maps of cellular recruitment of CTLs for two of the treatment groups. Top row shows cell maps in tumors, bottom row indicates cell maps in lymph nodes and surrounding fat pads.  $R_2^*$  maps were masked to tumors, lymph nodes and surrounding fat pads.

compared to mice treated with either DPX-R9F or DPX-R9F and anti-PD-1 (Figure 4c). At day 28, there were no significant differences in the number of SPIO-MLCs present in the tumor regardless of treatment. There was a significant difference in the change in SPIO-MLC recruitment between day 28 and day 21 (Figure 4d) between untreated mice and mice treated with anti-PD-1 (with similar, although not significant, differences between untreated mice and other treatment groups). Untreated mice had a significant decrease in the cellular density of SPIO-MLCs between day 21 and day 28 compared to treated groups. Representative recruitment maps of SPIO-MLCs can be seen in Figure 4e. Untreated mice seemed to have MLCs recruited more diffusely throughout the tumor (Figure 4e top row); however, there were no definitive differences in recruitment patterns. MLC recruitment to the lymph nodes is also clearly visualized throughout the lymph nodes in the bottom row of Figure 4e.

### DPX-R9F significantly increases recruitment of MLCs to treatment draining lymph node

We also evaluated how SPIO-labeled cells were recruited to the inguinal lymph nodes that either drain to the tumor (left lymph node; LLN) or drain to the site of DPX-R9F administration (right lymph node; RLN). In the RLN there were fewer SPIO-CTLs recruited in mice treated with anti-PD-1 and DPX-R9F than other groups, although the difference was not significant (Figure 5a). This was true at both day 21 and day 28. At day 21, there were significantly more SPIO-CTLs recruited to the RLN in the combination treatment versus anti-PD1 alone and there were also far fewer cells in the DPX-R9F and untreated groups, but the differences were not significant. There were significantly more SPIO-MLCs recruited to the RLN on day 28 in mice treated with the combination treatment compared to untreated mice (Figure 5c). In the LLN there was a significant change ( $p < .1$ ) in the number of SPIO-MLCs recruited at day

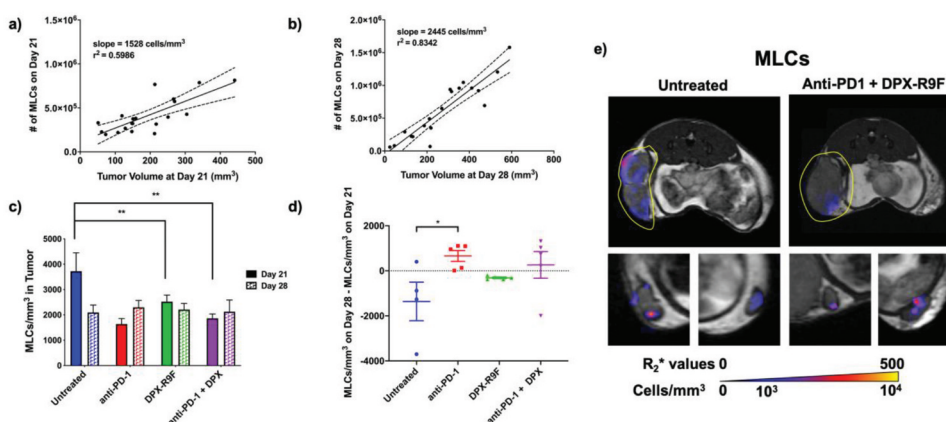


**Figure 4.** Treatment increases recruitment of MLCs to primary tumor between day 21 and day 28 & untreated mice have higher numbers of MLCs in the tumor at day 21. a) Individual graph showing numbers of MLCs recruited to the primary tumor at day 21 compared to the tumor volume at day 21. b) Same as A but for day 28. Both graphs in A and B are statistically non-zero according to linear regression analyses. c) The cellular density of MLCs recruited to the primary tumor for each treatment regime at both day 21 and day 28. d) The difference in cellular density of recruited MLCs between day 28 and day 21. \* indicates  $p < .1$ , \*\*  $p < .05$  according to t-test with Dunnett's correction for multiple comparisons. e) Representative maps of cellular recruitment of MLCs for two of the treatment groups. Top row shows cell maps in tumors, bottom row indicates cell maps in lymph nodes and surrounding fat pads.  $R_2^*$  maps were masked to tumors, lymph nodes and surrounding fat pads.

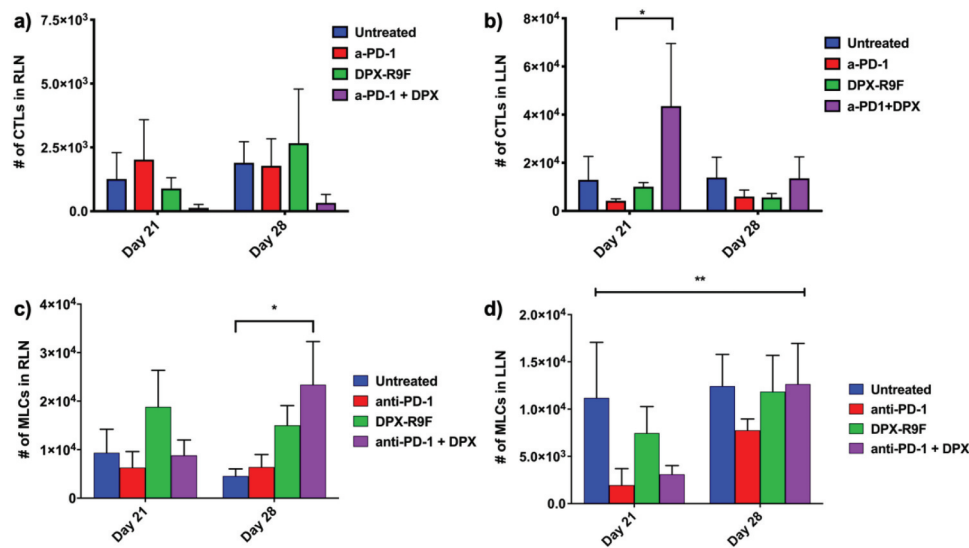


**Figure 5.** Treatment with DPX increases recruitment of CTLs to tumor-draining lymph node (LLN), increases recruitment of MLCs to treatment draining lymph node (RLN), and the number of MLCs recruited to the LLN increases with time with treatment. The number of CTLs recruited to a) the right lymph node (tumor-draining) or b) the left lymph node (DPX-draining) at days 21 and day 28 for each treatment. The number of MLCs recruited to c) the right lymph node (tumor-draining) or d) the left lymph node (DPX-draining) at days 21 and day 28 for each treatment.\* indicates  $p < .1$  according to t-test with Dunnett's correction for multiple comparisons; \*\* indicates that the mixed-model ANOVA found a significant effect due to time with  $p < .05$ .

21 compared to day 28 (Figure 5d) with SPIO-MLC recruitment increasing at day 28 for all groups except untreated mice.

### Migration of MLCs and CTLs was validated using biological assays

Immunohistochemistry and flow cytometry were used as two methods of validation of cellular migration to tumors and lymph nodes (Figure 6 and Supplementary Figure 2). Figure 6 shows histological images from the two groups that contrasted the most: the untreated mice and mice treated with the combination therapy. GFP+ cells are clearly visible in all tumor and LN tissues of mice that had either MLC and CTL injections, providing evidence that TurboSPI signals likely corresponds to cells injected through adoptive transfer. Due to the heterogeneity of cellular distributions and small areas viewed with microscopy, immunohistochemistry should not be taken as a direct representation of actual cell numbers. For more quantitative investigation, we did tissue dissociation followed by flow cytometry was used to demonstrate that GFP+ cells could be detected through another methodology than immunohistochemistry. As demonstrated in Supplementary Figure 3, we found, by flow cytometry, that on average, 20–50 GFP+ cells/50 000 events were visible in digested lymph nodes and that 0–500 GFP+ cells/1 million events were visible in digested tumors from untreated mice.

### Discussion

Novel immunotherapies are a rapidly expanding field of cancer research, yet there is a significant gap in our understanding of the mechanism(s) of action of these therapies that affects and delays their translation to the clinic. Molecular imaging technologies such as quantitative MRI

are key translational tools for getting these therapies to patients. In this work we demonstrated the ability of quantitative MRI, using the pulse sequence TurboSPI, to longitudinally monitor and quantify the recruitment of two types of immune cells to tumors and inguinal lymph nodes in response to treatment with immunotherapy.

Previous work by Weir et al.<sup>30</sup> demonstrated that anti-PD-1 combined with the peptide-based immunotherapy DPX-R9F offered potent anti-cancer control in the C3 tumor model. This work expands this study further by evaluating whether immune cell tracking via MRI can also be used to offer insights into immune cell recruitment in the tumor microenvironment and in the draining lymphatic system. This work also goes beyond confirmation of the Weir et al. study<sup>30</sup> and offers longitudinal data demonstrating *in vivo* infiltration of T cells in treated animals at two time points, whereas classical immunological assays such as ELISPOT or flow cytometry allow only “snapshots” of activity.

In this study, we found that adding DPX-R9F to anti-PD-1 increased the density of CD8 + T cells recruited to the tumor between day 21 and day 28, which is the period of time where tumors are generally undergoing rapid growth if treatment fails to control tumor growth in this tumor model. CD8 + T cells were also recruited in significantly larger numbers to the tumor-draining lymph node in mice treated with the combination therapy compared to all other groups. DPX-R9F alone appeared to trend toward increased recruitment of CD8 + T cells between day 21 and day 28, but the results were only statistically significant when anti-PD-1 was also used, indicating a potential cumulative effect of the combination. These results demonstrate the importance of the role that DPX-R9F plays in increasing the recruitment and activity of CD8 + T cells, particularly in combination with anti-PD-1, which has also been demonstrated elsewhere.<sup>8,30,35</sup>

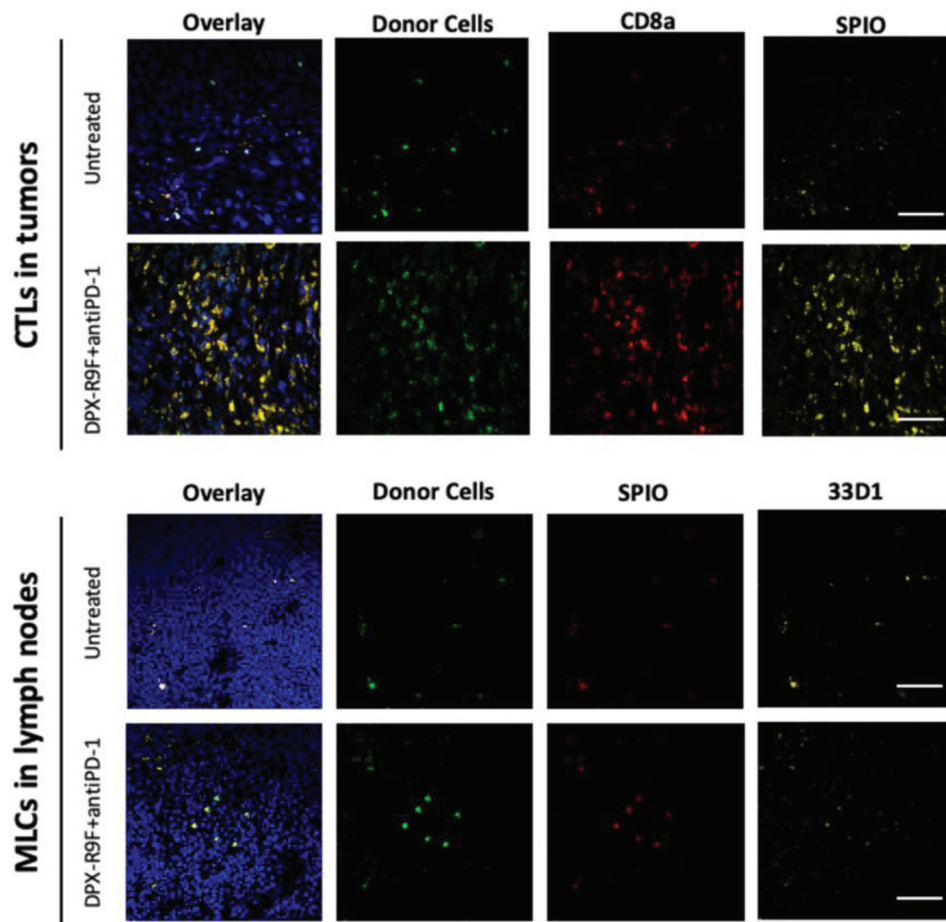


**Figure 6.** Histological validation of CTL and MLC migration. All tissues shown are from mice who had been either been untreated or treated with both DPX and anti-PD-1. Tumor (top panels) and lymph nodes (bottom panels) from recipient mice were frozen and sectioned for immunohistological staining with either CD8a+ PE (top panels) or stained with the dendritic cell marker 33D1 (bottom panels) followed by Alexa Fluor 633 secondary. Only injected cells isolated from B6-GFP+ mice were GFP+ and Rhodamine B+ for SPIO. Nuclei are stained with DAPI to show tissue morphology. The scale bar represents 50  $\mu$ m.

Additionally, we found that treatment with DPX-R9F (with or without anti-PD-1) also increased the migration of MLCs to the therapy-draining lymph node (RLN), while untreated tumors had higher recruitment of MLCs at day 21. While MLCs located in the RLN likely play an important role by presenting antigens to lymphocytes, recent work demonstrates that myeloid lineage cells, such as dendritic cells, found at the tumor site are functionally defective and can actually act as suppressor cells.<sup>36</sup> This would explain their large presence in untreated tumors. MLCs in anti-PD-1-treated mice were increasingly recruited to the tumor between day 21 and day 28. This change could potentially be linked to a more rapid increase in the suppressive tumor microenvironment causing any potential treatment effects to be overcome.

Immune cell recruitment changes were also evaluated at the individual level, particularly with respect to tumor growth. Not surprisingly, larger tumors lead to the recruitment of more immune cells. However, the recruitment rate does appear to change within treatment groups, and more notably, between time points. MLCs were recruited at a much higher rate per tumor volume at day 28 compared to day 21. In this study, the group sizes ( $n = 5$ ) were too small to obtain statistical significance regarding immune cell recruitment for each treatment group.

It should be noted that labeling with SPIO may slightly affect the phenotype of the immune cells, although not significantly. Labeling CD8 + T cells with SPIO appeared to slightly increase the expression of PD-1, TIM3, and CTLA-4 (supplementary Figure 1). A previous study<sup>27</sup> demonstrated that T cell cytotoxicity was not affected by labeling with SPIO, so it is not clear what effects these small phenotypic changes may have on cell behavior, but future experiments will assess other potential exhaustion markers.

We proceeded to validate the presence or absence of CTLs and MLCs in the tumor and draining lymphatic system by immunohistochemistry of frozen tumors and inguinal lymph nodes, and tumor dissociation followed by flow cytometry for analysis of GFP+ cells in tissue. Our strategy of using B6-GFP+ mice as donor mice for adoptive transfer into wild-type B6 mice proved to be extremely useful for validation of our MRI methods. We were able to provide dual detection and verification by correlating fluorescence from the Rhodamine B from the SPIO to the GFP fluorescence from the injected SPIO-cells in immunofluorescence. The GFP signal was useful for confirming the presence of adoptively transferred cells at the end of the study. Attempts were made to quantify the injected cells by means of tumor and LN dissociation followed by flow cytometry, but this proved challenging due to a significant decrease in cell viability



after tissue processing and so was not pursued. The higher proportion of GFP+ cells in lymph nodes is the likely result of less cell death during processing, since lymph nodes were mechanically dissociated into a single-cell suspension rather than being treated with enzymes like the tumor samples. The results from both MRI and immunofluorescence demonstrate that not only does DPX-R9F generate targeted T cell responses, but this treatment is able to drive T cells into the tumor (including cells that were adoptively transferred).

In this work, we were careful to describe one of our injected cell subsets as myeloid lineage cells (MLCs) as opposed to trying to define their specific subset. It has been increasingly acknowledged in recent literature that cells derived via culture of bone-marrow cells are more diverse than previously acknowledged, and that it is very difficult to distinguish between bone marrow-derived macrophages (BMDM) and bone marrow-derived dendritic cells (BMDCs).<sup>37</sup> Although our flow cytometry analysis indicates that approximately 80% of our MLCs were CD11c+, and that 80% of CD11c+ cells were MHCII+, indicating a likely DC phenotype, it is possible that the other proportion of the MLCs was BMDMs given that they are typically MHCII<sup>low</sup>. Regardless of their precise phenotype, based on MR results (and immunohistochemistry) it is likely that therapies based on DPX formulation are driving these particular cells to the therapy-draining lymph node (RLN) to act as antigen-presenting cells.

One limitation of this work is the dependence on the evaluation of group results as opposed to individual results. In order to validate this new quantitative technique, we wanted to concentrate on ensuring that immunological results were consistent with previous work. As such, we calculated immune cell numbers over the entire tumor or lymph node and compared these at the group level (except for cell recruitment versus tumor volume graphs). This ignores the rich 3D data that is currently not being exploited, such as the location of immune cells within the tumor microenvironment. We consistently observed very similar patterns of immune cell recruitment within tumors, with cells generally located on tumor peripheries with limited infiltration into the tumor core for CD8 + T cells. MLCs had more varied migration patterns with larger cell numbers generally present within the central region of the tumor. Future work will include the use of machine learning techniques to evaluate more complex image metrics (such as location and presence of clusters) of these 3D cell density maps and evaluate whether any of these metrics are predictive of biological responses or more precise indicators of points of treatment failure.

It would be valuable in future studies to obtain more time points, particularly at a somewhat finer resolution, such as every 3–4 days from day 14 to day 35. This would allow more precise probing of immunological responses occurring at the individual level, especially over the time frame where immune cell tumor evasion is dominant. Given that two time points allowed us to monitor significant changes in immune cell recruitment between groups, more time points would allow us to evaluate whether CD8 + T cell recruitment would eventually peak in the combination groups, and whether the differential recruitment of MLCs correlates with different phases of tumor growth. Understanding cellular kinetics can inform optimization of combination therapies with respect to sequence and timing.

## Conclusion

This work demonstrates that quantitative MRI cell tracking can be used to accurately monitor changes in CD8 + T cells and myeloid lineage cell recruitment over time in response to a variety of immunotherapies with results that are consistent with more traditional biological techniques. TurboSPI is an MRI pulse sequence that can quantitatively and longitudinally monitor immunological responses in individual tumor-bearing mice in a variety of cancer models. We were able to demonstrate, using TurboSPI, that CD8 + T cell recruitment to C3 cervical cancer tumors and the respective treatment draining lymph node increased over time in response to treated with the combination of DPX-R9F and anti-PD-1. This method offers advantages over traditional techniques used for evaluating treatment efficacy, such as flow cytometry, polymerase chain reaction for gene expression, or tumor-infiltrating lymphocyte assays, by allowing us to monitor immunological changes at multiple sites over time, addressing the individual nature of immunotherapies.

## Acknowledgments

The authors would like to thank Caitrin Sobey-Skelton for help with text, data analysis, and with some biological assays. We would also like to thank Raj Rajagopalan for assistance in preparing the DPX-based immunotherapies.




## Disclosure statement

At the time of writing this manuscript, MLT, GW, and MS were employees of IMV Inc., who manufactures DPX-based immunotherapies. KDB also had a research contract with IMV for an unrelated project.

## Funding

KDB would like to acknowledge that this work was funded by the Nova Scotia Health Research Foundation (NSHRF) in the form of an establishment grant and the National Sciences and Engineering Research Council (NSERC) in the form of a Discovery grant. WMK would like to acknowledge funding from the NIH; R01 CA74397.

## ORCID

Genevieve Weir  <http://orcid.org/0000-0002-6285-7187>  
 Marianne Stanford  <http://orcid.org/0000-0003-0432-3707>  
 Kimberly D. Brewer  <http://orcid.org/0000-0001-7973-0126>

## References

1. Weiss L, Huemer F, Mlineritsch B, Greil R. Immune checkpoint blockade in ovarian cancer. *Memo Springer Vienna*. 2016;9:82–84.
2. Ojalvo LS, Nichols PE, Jelovac D, Emens LA. Emerging immunotherapies in ovarian cancer. *Discov Med*. 2015;20:97–109.
3. Ferris RPD-1. targeting in cancer immunotherapy. *Cancer*. 2012;119:E1–E3. doi:10.1002/cncr.27832.
4. Baxevasis CN, Perez SA, Papamichail M. Combinatorial treatments including vaccines, chemotherapy and monoclonal antibodies for cancer therapy. *Cancer Immunol Immunother*. 2009;58(3):317–324. doi:10.1007/s00262-008-0576-4.
5. Sharma P, Allison JP. Immune checkpoint targeting in cancer therapy: toward combination strategies with curative potential. *Cell*. 2015;161(2):205–214. doi:10.1016/j.cell.2015.03.030.
6. Berinstein NL, Karkada M, Oza AM, Odunsi K, Vilella JA, Nemunaitis JJ, Morse MA, Pejovic T, Bentley J, Buyse M, et al.

- Survivin-targeted immunotherapy drives robust polyfunctional T cell generation and differentiation in advanced ovarian cancer patients. *Oncoimmunology*. 2015;4(8):e1026529. doi:10.1080/2162402X.2015.1026529.
7. Garg H, Suri P, Gupta JC, Talwar GP, Dubey S. Survivin: a unique target for tumor therapy. *Cancer Cell Int BioMed Central*. 2016;16:49. doi:10.1186/s12935-016-0326-1.
  8. Karkada M, Weir GM, Quinton T, Sammat L, MacDonald LD, Grant A, Liwski R, Juskevicius R, Sinnathamby G, Philip R, et al. A novel breast/ovarian cancer peptide vaccine platform that promotes specific type-1 but not Treg/Tr1-type responses. *J Immunother*. 2010;33(3):250–261. doi:10.1097/CJI.0b013e3181c1f1e9.
  9. Berinstein NL, Karkada M, Morse MA, Nemunaitis JJ, Chatta G, Kaufman H, Odunsi K, Nigam R, Sammat L, MacDonald LD, et al. First-in-man application of a novel therapeutic cancer vaccine formulation with the capacity to induce multi-functional T cell responses in ovarian, breast and prostate cancer patients. *J Transl Med BioMed Central*. 2012;10:156. doi:10.1186/1479-5876-10-156.
  10. Weir GM, Hrytsenko O, Stanford MM, Berinstein NL, Karkada M, Liwski RS, Mansour M. Metronomic cyclophosphamide enhances HPV16E7 peptide vaccine induced antigen-specific and cytotoxic T-cell mediated antitumor immune response. *Oncoimmunology*. 2014;3:e953407.
  11. Medicines in development for cancer. Pharmaceutical research and manufacturers of America. 2015 Sep 1–4.
  12. Ott PA, Hodi FS, Kaufman HL, Wigginton JM, Wolchok JD. Combination immunotherapy: a road map. *J Immunother Cancer*. 2017;5(1):16. doi:10.1186/s40425-017-0218-5.
  13. Messenheimer DJ, Jensen SM, Afentoulis ME, Wegmann KW, Feng Z, Friedman DJ, Gough MJ, Urba WJ, Fox BA. Timing of PD-1 blockade is critical to effective combination immunotherapy with Anti-OX40. *Clin Cancer Res*. 2017;23(20):6165–6177. doi:10.1158/1078-0432.CCR-16-2677.
  14. Zeelen C, Paus C, Draper D, Heskamp S, Signore A, Galli F, Griessinger C, Aarntzen EH. In-vivo imaging of tumor-infiltrating immune cells: implications for cancer immunotherapy. *Q J Nucl Med Mol Imaging*. 2018;62:56–77.
  15. Ehlerding EB, England CG, McNeel DG, Cai W. Molecular imaging of immunotherapy targets in cancer. *J Nucl Med*. 2016;57(10):1487–1492. doi:10.2967/jnumed.116.177493.
  16. Li A, Wu Y, Tang F, Li W, Feng X, Yao Z. In Vivo magnetic resonance imaging of CD8+ T lymphocytes recruiting to glioblastoma in mice. *Cancer Biother Radiopharm*. 2016;31(9):317–323. doi:10.1089/cbr.2016.2061.
  17. Kikuchi M, Clump DA, Srivastava RM, Sun L, Zeng D, Diaz-Perez JA, Anderson CJ, Edwards WB, Ferris RL. Preclinical immunoPET/CT imaging using Zr-89-labeled anti-PD-L1 monoclonal antibody for assessing radiation-induced PD-L1 upregulation in head and neck cancer and melanoma. *Oncoimmunology*. 2017;6:e1329071. doi:10.1080/2162402X.2017.1329071.
  18. Chatterjee S, Lesniak WG, Miller MS, Lisok A, Sikorska E, Wharram B, Kumar D, Gabrielson M, Pomper MG, Gabelli SB, et al. Rapid PD-L1 detection in tumors with PET using a highly specific peptide. *Biochem Biophys Res Commun*. 2017;483(1):258–263. doi:10.1016/j.bbrc.2016.12.156.
  19. Keu KV, Witney TH, Yaghoubi S, Rosenberg J, Kurien A, Magnusson R, Williams J, Habte F, Wagner JR, Forman S, et al. Reporter gene imaging of targeted T cell immunotherapy in recurrent glioma. *Sci Transl Med*. 2017;9(373):eaag2196. doi:10.1126/scitranslmed.aag2196.
  20. Kircher MF, Allport JR, Graves EE, Love V, Josephson L, Lichtman AH, Weissleder R. In vivo high resolution three-dimensional imaging of antigen-specific cytotoxic T-lymphocyte trafficking to tumors. *Cancer Res*. 2003;63:6838–6846.
  21. Makela AV, Gaudet JM, Foster PJ. Quantifying tumor associated macrophages in breast cancer: a comparison of iron and fluorine-based MRI cell tracking. *Sci Rep*. 2017;7(1):1–9. doi:10.1038/srep42109.
  22. Zhang X, de Chickera SN, Willert C, Economopoulos V, Noad J, Rohani R, Wang AY, Levings MK, Scheid E, Foley R, et al. Cellular magnetic resonance imaging of monocyte-derived dendritic cell migration from healthy donors and cancer patients as assessed in a scid mouse model. *Cytotherapy*. 2012;13:1234–1248. doi:10.3109/14653249.2011.605349.
  23. Srinivas M, Aarntzen EHJG, Bulte JWM, Oyen WJ, Heerschap A, de Vries IJM, Figdor CG. Imaging of cellular therapies. *Adv Drug Deliv Rev*. 2010;62(11):1080–1093. doi:10.1016/j.addr.2010.08.009.
  24. Smirnov P, Lavergne E, Gazeau F, Lewin M, Boissonnas A, Doan BT, Gillet B, Combadière C, Combadière B, Clément O, et al. In vivo cellular imaging of lymphocyte trafficking by MRI: A tumor model approach to cell-based anticancer therapy. *Magn Reson Med*. 2006;56(3):498–508. doi:10.1002/mrm.20996.
  25. Mallett CL, McFadden C, Chen Y, Foster PJ. Migration of iron-labeled KHYG-1 natural killer cells to subcutaneous tumors in nude mice, as detected by magnetic resonance imaging. *Cytotherapy*. 2012;14(6):743–751. doi:10.3109/14653249.2012.667874.
  26. Korchinski DJ, Taha M, Yang R, Nathoo N, Dunn JF. Iron Oxide as an MRI Contrast Agent for Cell Tracking. *Magn Reson Insights*. 2015;8:15–29.
  27. Tremblay M-L, Davis C, Bowen CV, Stanley O, Parsons C, Weir G, Karkada M, Stanford MM, Brewer KD. Using MRI cell tracking to monitor immune cell recruitment in response to a peptide-based cancer vaccine. *Magn Reson Med*. 2017;342:1432.
  28. Rioux JA, Brewer KD, Beyea SD, Bowen CV. Quantification of superparamagnetic iron oxide with large dynamic range using TurboSPI. *J Magn Reson*. 2012;216:152–160. doi:10.1016/j.jmr.2012.01.017.
  29. Rioux JA, Beyea SD, Bowen CV. 3D single point imaging with compressed sensing provides high temporal resolution  $R_2^*$  mapping for in vivo preclinical applications. *MAGMA*. 2017;30:41–55. doi:10.1007/s10334-016-0583-y.
  30. Weir GM, Hrytsenko O, Quinton T, Berinstein NL, Stanford MM, Mansour M. Anti-PD-1 increases the clonality and activity of tumor infiltrating antigen specific T cells induced by a potent immune therapy consisting of vaccine and metronomic cyclophosphamide. *J Immunother Cancer*. 2016;4(1):68. doi:10.1186/s40425-016-0169-2.
  31. Feltkamp MC, Smits HL, Vierboom MP, Minnaar RP, de Jongh BM, Drijfhout JW, Schegier JT, Melief CJM, Kast WM. Vaccination with cytotoxic T lymphocyte epitope-containing peptide protects against a tumor induced by human papillomavirus type 16-transformed cells. *Eur J Immunol*. 1993;23(9):2242–2249. doi:10.1002/eji.1830230929.
  32. Brewer KD, Weir GM, Dude I, Davis C, Parsons C, Penwell A, Rajagopalan R, Sammat L, Bowen CV, Stanford MM, et al. Unique depot formed by an oil based vaccine facilitates active antigen uptake and provides effective tumour control. *J Biomed Sci*. 2018;25(1):7. doi:10.1186/s12929-018-0413-9.
  33. Schindelin J, Rueden CT, Hiner MC, Eliceiri KW. The ImageJ ecosystem: an open platform for biomedical image analysis. *Mol Reprod Dev*. 2015;82(7–8):518–529. doi:10.1002/mrd.22489.
  34. O'Brien-Moran Z, Bowen CV, Rioux JA, Brewer KD. Cell density quantification with TurboSPI:  $R_2^*$  mapping with compensation for off-resonance fat modulation. *MAGMA*. 2019;3:250.
  35. Weir GM, Liwski RS, Mansour M. Immune Modulation by Chemotherapy or Immunotherapy to Enhance Cancer Vaccines. *Cancers*. 2011;3(3):3114–3142. doi:10.3390/cancers3033114.
  36. Veglia F, Gabrilovich DI. Dendritic cells in cancer: the role revisited. *Curr Opin Immunol*. 2017;45:43–51. doi:10.1016/j.coi.2017.01.002.
  37. Na YR, Jung D, Gu GJ, Seok SH. GM-CSF grown bone marrow derived cells are composed of phenotypically different dendritic cells and macrophages. *Mol Cells*. 2016;39:734–741.